

High-Strength Hydrogel Attachment through Nanofibrous Reinforcement

Jiacheng Zhao, Alina Kirillova, Cambre N. Kelly, Heng Xu, William J. Koshut, Feichen Yang, Ken Gall, and Benjamin J. Wiley*

The repair of a cartilage lesion with a hydrogel requires a method for long-term fixation of the hydrogel in the defect site. Attachment of a hydrogel to a base that allows for integration with bone can enable long-term fixation of the hydrogel, but current methods of forming bonds to hydrogels have less than a tenth of the shear strength of the osteochondral junction. This communication describes a new method, nanofiber-enhanced sticking (NEST), for bonding a hydrogel to a base with an adhesive shear strength three times larger than the state-of-the-art. An example of NEST is described in which a nanofibrous bacterial cellulose sheet is bonded to a porous base with a hydroxyapatite-forming cement followed by infiltration of the nanofibrous sheet with hydrogel-forming polymeric materials. This approach creates a mineralized nanofiber bond that mimics the structure of the osteochondral junction, in which collagen nanofibers extend from cartilage into a mineralized region that anchors cartilage to bone.

available, allows immediate weight-bearing, has short recovery times, and has low long-term failure rates.

Based on the limitations of biological approaches to cartilage restoration, there are ongoing efforts to perform focal joint resurfacing with durable orthopedic materials (e.g., cobalt-chromium alloy) to fill chondral or osteochondral defects.^[8,9] A primary concern with these implants is that they do not match the tribology and mechanical response of native cartilage, resulting in abnormal stress and opposing surface wear that causes joint degeneration.^[10,11] Incorrect placement of these implants can lead to severe damage of the opposing cartilage surface.^[12] A review of the results of focal metallic inlay resurfacing prosthesis indicates 20% of patients have to be converted to arthroplasty after 4 years.^[13]

Articular cartilage lesions, which most often occur in the knee, have a limited intrinsic ability to heal and are associated with joint pain and disability.^[1] Common strategies for cartilage restoration, such as microfracture, have high failure rates ($\approx 50\%$ at 10 years) and prolonged rehabilitation times (12–18 months).^[2–4] Implantation of fresh osteochondral allografts can allow immediate weight-bearing and, with a survivorship of 82% at 10 years, is the most successful strategy for treatment of cartilage defects.^[5,6] Unfortunately, the small supply of fresh allografts limits the number of these procedures to around 1% of all cartilage repair surgeries. Decellularized, shelf-stable allografts have very high failure rates (72% in 2 years) characterized by delamination of the articular cartilage in the graft due to collagen degradation.^[7] There is a clear need for a cartilage repair method that is widely

Hydrogels can be created to have a similar stiffness and coefficient of friction as cartilage, thereby addressing concerns related to abnormal stress and wear.^[14] However, there is currently no way to secure a hydrogel into a cartilage defect site with the same shear strength as the osteochondral junction (7.25 ± 1.35 MPa).^[15] One of the strongest tissue adhesives is cyanoacrylate, which has been reported to achieve a lap shear strength of 0.7 MPa between two pieces of cartilage.^[16] In contrast, cyanoacrylate bonds nylon to nylon and steel to steel with a shear strength of 2.8 and 7.3 MPa,^[17,18] respectively. This comparison suggests that the presence of interfacial water in cartilage (cartilage is 60–85% water by weight)^[19] hinders the creation of a stronger bond. Indeed, mussel and spider glues have mechanisms to displace interfacial water in order to create stronger bonds.^[20,21] Biological approaches to removal of interfacial water have inspired the development of dry, tissue-bonding double-sided tape and strong underwater adhesives.^[22–24] Thus, the removal of interfacial water is an important strategy for forming strong bonds to hydrogels.

Another strategy to form strong bonds with hydrogels is to mimic the bonding of cartilage to bone.^[25] The osteochondral junction is characterized by a layer of collagen nanofibers extending from the deep zone of cartilage into a mineralized region that is attached to subchondral bone through an interdigitated interface.^[26,27] In this way, the collagen nanofibers that give cartilage its excellent tensile strength also anchor it to the surface of bone.

J. Zhao, H. Xu, F. Yang, Prof. B. J. Wiley
Department of Chemistry
Duke University
124 Science Drive, Box 90354, Durham, NC 27708, USA
E-mail: Benjamin.wiley@duke.edu

Dr. A. Kirillova, Dr. C. N. Kelly, W. J. Koshut, Prof. K. Gall
Department of Mechanical Engineering and Materials Science
Duke University
144 Hudson Hall, Box 90300, Durham, NC 27708, USA

 The ORCID identification number(s) for the author(s) of this article can be found under <https://doi.org/10.1002/adhm.202001119>

DOI: 10.1002/adhm.202001119

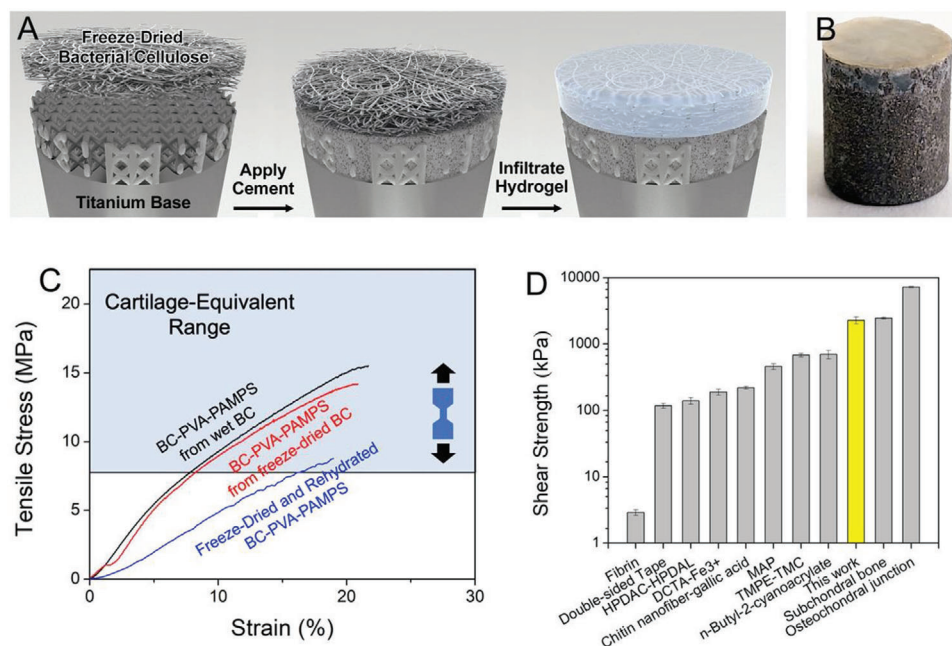


Figure 1. A) Illustration of Nanofiber-Enhanced Sticking (NEST). B) Image of a hydrogel bonded to a titanium plug with the NEST method. C) Tensile stress–strain curves of BC-PVA-PAMPS hydrogels prepared from wet and freeze-dried BC, as well as freeze-dried and rehydrated BC-PVA-PAMPS (where BC is bacterial cellulose, PVA is polyvinyl alcohol, and PAMPS is poly(2-acrylamido-2-methyl-1-propanesulfonic acid sodium salt)). D) Shear strength obtained for the NEST method using an α -tricalcium phosphate (α -TCP) cement compared to state-of-the-art hydrogel adhesives and the osteochondral junction.

This communication describes a new approach, nanofiber-enhanced sticking (NEST), that combines the strategies of water removal and nanofiber mineralization. The essence of this strategy, illustrated in **Figure 1A,B**, is to first attach a dry nanofibrous layer to a porous base of interest before infiltration of the hydrogel components. In this way, the adhesive or cement can penetrate into the porous nanofibrous network and create an interdigitating bond without the interference of water.

A recently reported cartilage-equivalent hydrogel composed of bacterial cellulose (BC), polyvinyl alcohol (PVA), poly(2-acrylamido-2-methyl-1-propanesulfonic acid sodium salt) (PAMPS), and 59% water proved to be an excellent candidate for this strategy.^[14] The BC nanofibers in the hydrogel provide a source of tensile strength similar to collagen nanofibers in cartilage. Although this hydrogel was previously prepared from wet BC, we found that BC could be freeze-dried and infiltrated with PVA and PAMPS to create a hydrogel with nearly the same tensile strength (12.37 ± 3.83 MPa) as one that is not freeze-dried (13.42 ± 3.86 MPa). As shown in **Figure 1C**, the tensile strengths of hydrogels prepared by the infiltration of wet or freeze-dried BC are well within the range of tensile strengths reported for human cartilage (8.1–40 MPa).^[28] In contrast, if the full BC-PVA-PAMPS hydrogel is freeze-dried, the tensile strength is only 9.62 ± 2.63 MPa. This result suggests the nanofibrous BC can accommodate the formation of ice crystals by fiber displacement without fiber fracture, whereas the molecularly cross-linked hydrogel network is irreversibly damaged by ice crystal formation.

Figure 1D compares the maximum adhesive shear strength achieved for the NEST strategy with the previous work (see also

Table S1, Supporting Information).^[16,29–44] Mimicking the osteochondral junction, we mineralized the BC nanofibers with a hydroxyapatite-forming cement to achieve an adhesive shear strength of 2.28 ± 0.27 MPa, a three-fold increase over the state-of-the-art. This is lower than the shear strength reported for the human osteochondral junction (7.25 ± 1.35 MPa),^[15] but is similar to the shear strength reported for the bovine osteochondral junction (2.6 ± 0.58 MPa)^[45] and human subchondral bone (2.45 ± 0.85).^[15] The rest of this communication describes the experiments performed to arrive at this shear strength.

We focused on the use of α -tricalcium phosphate (α -TCP) as a hydroxyapatite-forming cement for attachment of the hydrogel due to its biocompatibility, osteoconductivity, and shear strength that exceeds that of cyanoacrylate.^[46,47] By itself, α -TCP does not act as an adhesive. Thus, we tested the addition of 10 wt% phosphoserine (PPS), a component of sandcastle worm glue,^[48] to promote adhesion. Hydroxyapatite is brittle and benefits from reinforcement,^[49] so we tested the addition of 12 wt% stainless-steel powder (SSP) with an average particle size of 150 μm to hinder crack propagation.

To create samples for adhesive shear testing and study of the cement by itself, a dry cement mixture consisting of 0.040 g PPS, 0.312 g of α -TCP, and 0.048 g of SSP was placed into a small dish, 0.140 mL of water was added, and the powder was rapidly mixed with the water. Powders were also created without PPS or SSP to examine the effects of these additives. Approximately 0.150 mL of the wet cement mixture was added on top of a porous titanium plug in a metal die with an inner diameter of 6 mm. The plug consisted of a titanium alloy (Ti6Al4V) topped with a 1 mm thick layer of 3D printed struts with a porosity of 70%. **Figure 1A**

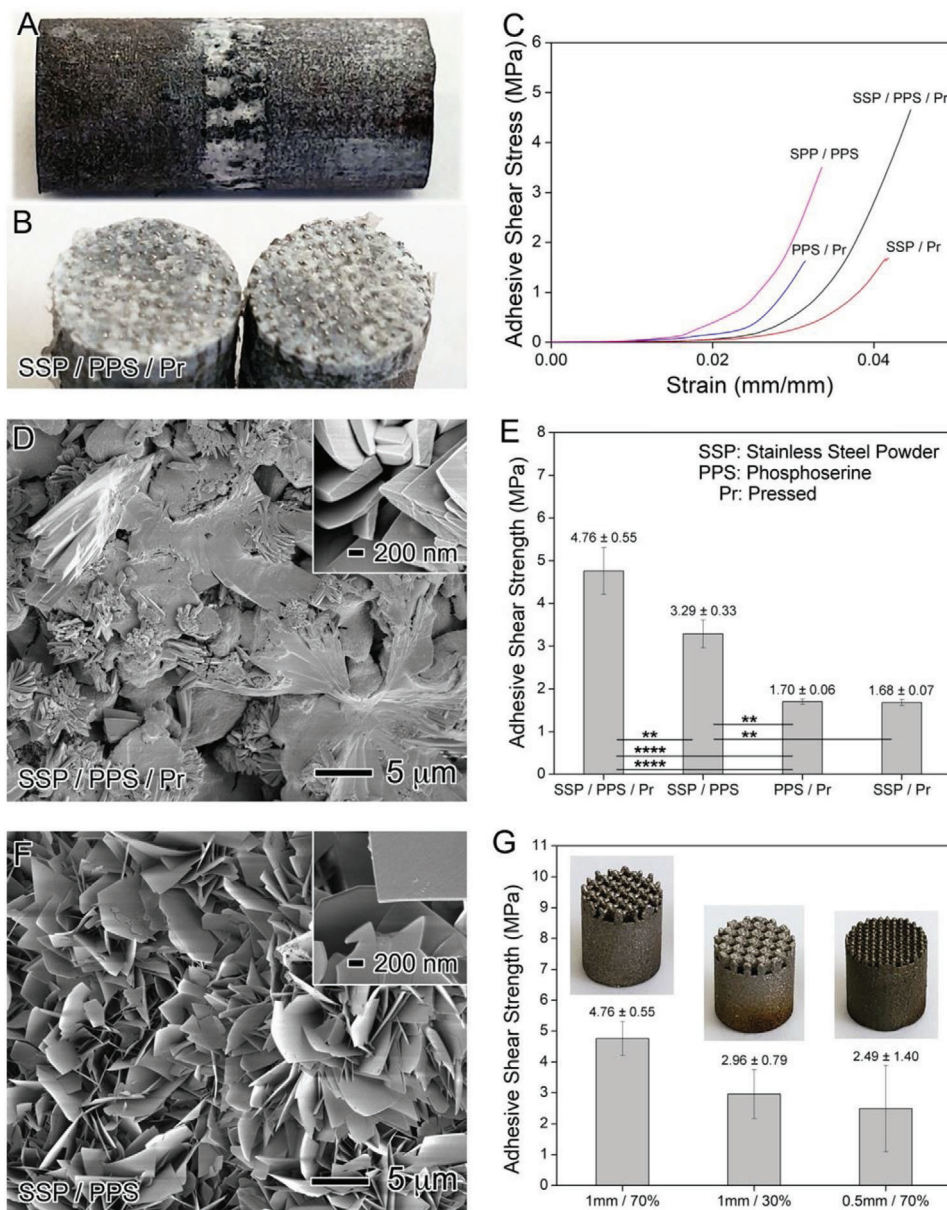


Figure 2. Image of an α -tricalcium phosphate (α -TCP) cement sample A) before and B) after shear testing. C) Stress–strain curves for different cement compositions. D) Scanning electron microscopy (SEM) image of the fracture surface for the sample containing stainless-steel powder (SSP) and phosphoserine (PPS) that was pressed at 250 MPa. E) Effect of composition and pressing on adhesive shear strength ($n = 3$, mean \pm SD). F) SEM image of the fracture surface for the sample made with SSP and PPS without pressing. G) Effect of the strut structure on adhesive shear strength ($n = 3$). The p -values from one-way ANOVA are labeled as $*p < 0.05$, $**p < 0.01$, $***p < 0.001$, and $****p < 0.0001$.

includes a rendering of the strut structure in the computer-aided design (CAD) file used for 3D printing. Scanning electron microscopy (SEM) images of the powder used for 3D printing and the printed strut structure are shown in Figure S1 (Supporting Information). The titanium plug is 6 mm in diameter and 6.35 mm in height. A second titanium plug was immediately placed into the die with the porous layer in contact with the wet cement, and the sandwich structure was pressed together for 1 h at 250 MPa. Samples were also made without the application of pressure to test the effect of this step on shear strength. The application of pressure has previously been demonstrated to reduce the poros-

ity of calcium phosphate cements, thereby improving their compression and flexural strength,^[50–52] but the effect of pressure on the adhesive shear strength of an α -TCP cement has not been reported. The sample was placed into water at 85 °C for at least 24 h to facilitate the transformation of α -TCP into hydroxyapatite and was stored in water until just prior to shear testing. Figure S2 (Supporting Information) shows the X-ray diffraction (XRD) pattern of the α -TCP cement before and after hydration, confirming the conversion to hydroxyapatite.^[53] Figure 2A shows an image of the sandwich structure in which the α -TCP cement bonds two titanium plugs.

Shear testing was performed on a Test Resources 830LE63 Axial Torsion Test Machine equipped with a 100 lb load cell and a custom-made shear testing fixture (see Figure S3, Supporting Information). A cross-head displacement rate of 2 mm min^{-1} was used for all the measurements.

Figure 2B is an optical image of the cement fracture surface after shear testing, indicating cohesive failure. This particular sample contained SSP, PPS, and was pressed, but all cement samples exhibited a similar cohesive fracture surface. A previous study of a PPS-containing α -TCP cement demonstrated that failure can be partially adhesive for bonding smooth titanium plugs but becomes cohesive when the cementitious bond is made between porous titanium surfaces.^[14]

Figure 2C shows typical stress–strain curves for shear testing of cements with different compositions, and Figure 2D shows the average and standard deviation of the strength for three samples of each composition. The cement composition with the highest adhesive shear strength ($4.76 \pm 0.55 \text{ MPa}$) was pressed at 250 MPa and contained both SSP and PPS, in addition to the α -TCP cement. Without the pressing step, the adhesive shear strength decreased to $3.29 \pm 0.33 \text{ MPa}$. The SEM image of the fracture surface for the pressed sample in Figure 2C shows the hydroxyapatite crystals at the fracture surface were thicker than the flake-like hydroxyapatite crystals that grew in samples that were not pressed (Figure 2E). Both surfaces differ substantially in morphology from the spheroidal α -TCP cement particles (Figure S4, Supporting Information). Thus the application of pressure not only changes the porosity but also the crystal morphology of the hydroxyapatite in the cement, with the stronger sample consisting of a thicker hydroxyapatite crystal morphology.

Without PPS, the adhesive shear strength decreased to $1.68 \pm 0.07 \text{ MPa}$. Without the SSP, the adhesive shear strength decreased to $1.70 \pm 0.06 \text{ MPa}$. Thus, SSP, PPS, and mechanical pressing were all necessary to maximize the adhesive shear strength of the cement.

Next, we studied how the structure of the 3D printed titanium layer affected the shear strength between two titanium plugs. Two changes were made: 1) decreasing the porosity from 70% to 30% and 2) decreasing the thickness of the strut layer from 1 to 0.5 mm. As shown in Figure 2F, both changes led to a decrease in the adhesive shear strength (although the decrease was not statistically significant), so the 1-mm-thick layer with a porosity of 70% was used for the rest of the experiments.

After optimizing the adhesive shear strength of the cement and the structure of the porous titanium layer, we studied the attachment of the titanium plugs to the hydrogel in a sandwich structure. Testing was performed with a cement composed of 10 wt% PPS, 78 wt% α -TCP, and 12 wt% SSP. The cement mixture consisting of 0.080 g PPS, 0.624 g of α -TCP, and 0.096 g of SSP was placed into a small dish, 0.280 mL of water was added, and the powder was rapidly mixed with the water. Then 0.150 mL of the wet cement mixture was added on top of the porous titanium plug in the die. The BC sheet was placed on top of the cement in the die, and an additional 0.150 mL of the wet cement mixture was added on top of the BC sheet. A second porous titanium plug was then placed on top of the BC sheet in the die to create a sandwich structure. The sandwich structure was pressed for 1 h at 250 MPa. The sample was placed into water at 85 °C for 24 h to facilitate the transformation of α -TCP into hydroxyapatite.

The sample was then placed into a hydrothermal reactor with a mixture of PVA (40 wt%) and DI water (60 wt%) to infiltrate PVA into the BC layer. The sample was frozen at -78 °C and thawed to room temperature to further increase the strength of the PVA hydrogel. The sample was then soaked in a solution containing AMPS (30 wt%), cross-linker (*N,N'*-methylenebisacrylamide, $60 \times 10^{-3} \text{ M}$), and heat initiator (I2959, $50 \times 10^{-3} \text{ M}$) for 24 h. The hydrogel was heat cured at 60 °C for 8 h and the sample was soaked in DI water for at least 24 h. An image of the finished sample is shown in Figure 3A.

An image of the fracture surface after adhesive shear testing is shown in Figure 3B. For the fracture surface between the two titanium plugs in Figure 2B, the titanium prongs are visible through the cement, suggesting that the metal prongs were in contact prior to fracture. In contrast, for the fracture surface with the BC-PVA-PAMPS hydrogel between the titanium plugs in Figure 3B, the titanium prongs are not visible. Instead, the white, fibrous BC layer is covering the prongs on the right plug, and the hydrogel infiltrated into the remaining BC is covering the prongs on the left. This shows that the hydrogel completely penetrated through the BC layer in between the plugs. This fracture surface, as well as other similar fracture surfaces not shown, also suggests that fracture took place close to the interface between the hydrogel and cement in the BC layer. This may be due to stress concentration at the interface between the relatively soft hydrogel and hard cement. Previous studies of shear fracture of the osteochondral junction similarly show that fracture of the osteochondral junction occurs at the tidemark, i.e., the border between cartilage and mineralized cartilage, presumably due to stress concentration at this interface.^[45] Figure 3D shows SEM images of the left and right fracture surfaces in Figure 3B, showing the presence of BC and hydrogel on both surfaces. We could not observe hydroxyapatite at the fracture surface after hydrogel infiltration.

Figure 3C shows typical stress–strain curves for different hydrogel compositions, and Figure 3E shows the adhesive shear strength and standard deviation of three samples for each condition. With BC only in between the two titanium plugs, the adhesive shear strength was $0.58 \pm 0.23 \text{ MPa}$, eight times lower than the shear strength of the cement without the BC. This again indicates the cement is attached to the BC layer rather than forming a continuous bond through the BC layer. We note that, as shown by the SEM image in Figure S4 (Supporting Information), the size of the α -TCP cement particles is $6.6 \pm 4.9 \text{ }\mu\text{m}$, which is much larger than the pores in the BC layer. Therefore, even though a large pressure is applied to the sandwich structure, the α -TCP particles did not completely penetrate through the BC layer. To confirm this, we created disks consisting of BC pressed into the cement at 250 MPa, put them into water at 85 °C for 24 h to form hydroxyapatite, and broke the disks in half to image the BC-cement interface. Figure 3F shows hydroxyapatite crystals can be found up to about 10 microns from the cement-BC interface, with their frequency decreasing with increasing distance from the interface. This interface shows that the BC is indeed mineralized by the hydroxyapatite. The hydroxyapatite did not extend into the BC beyond about 10 microns. Figure S5 (Supporting Information) shows the BC 40 microns from the interface with cement is completely devoid of hydroxyapatite.

Infiltration of PVA into the BC layer increased the strain at failure, but not the adhesive shear strength. Infiltration of PAMPS

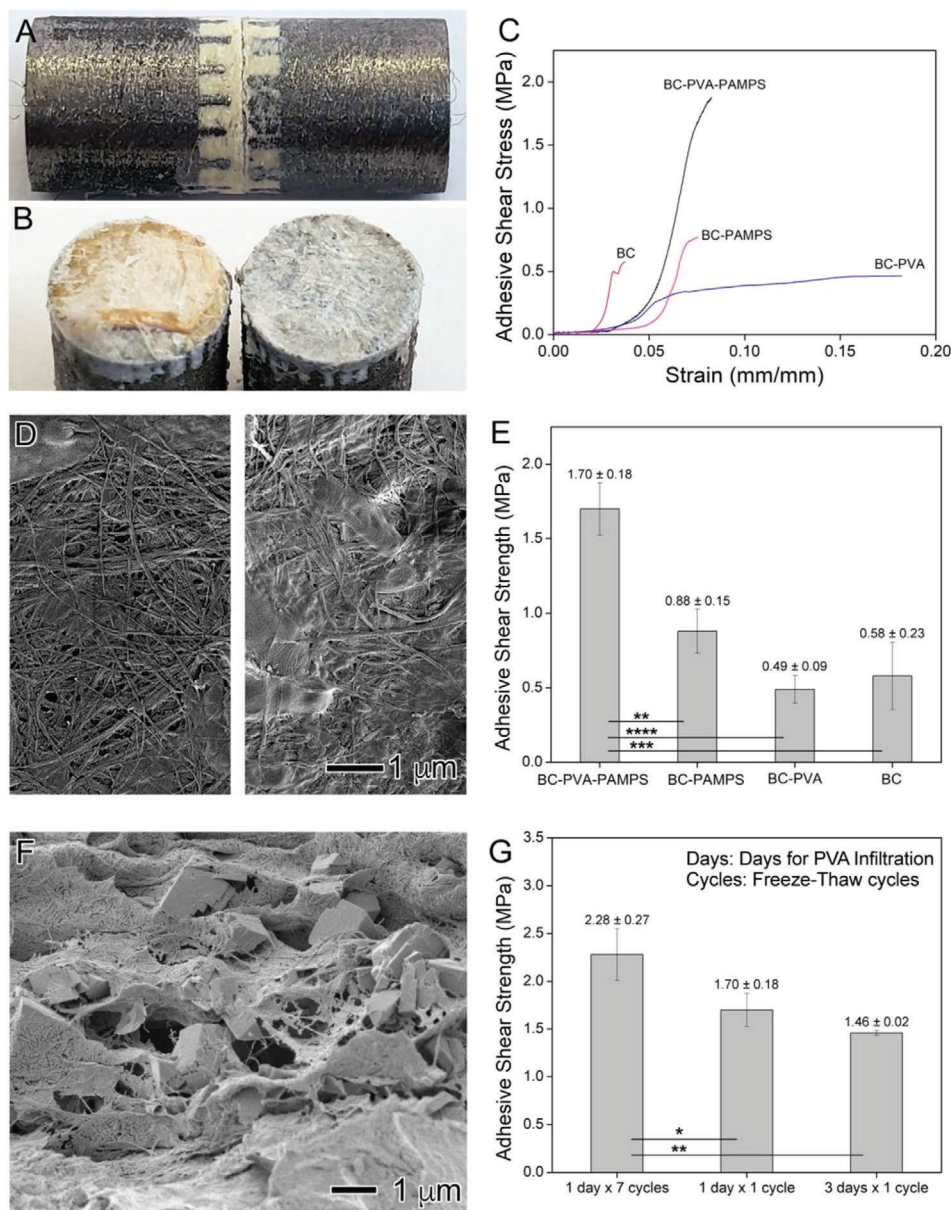


Figure 3. Image of sample for testing hydrogel-cement adhesive shear strength A) before and B) after shear testing. C) Typical stress–strain curves for hydrogels with different compositions. D) Scanning electron microscopy (SEM) images of the fracture surfaces in (B). E) Adhesive shear strength and standard deviation of different hydrogel compositions ($n = 3$). F) Cross-section SEM image of hydroxyapatite mineralizing the bacterial cellulose (BC) nanofibers. G) Effect of the hydrogel processing on adhesive shear strength ($n = 3$). The p -values from one-way ANOVA are labeled as $*p < 0.05$, $**p < 0.01$, $***p < 0.001$, and $****p < 0.0001$.

into the BC layer also did not significantly increase the strength and led to a smaller increase in the strain at failure than PVA due to the more brittle nature of the PAMPS hydrogel.^[14] However, the infiltration of both PVA and PAMPS into the BC layer lead to an increase in the adhesive shear strength to 1.70 ± 0.18 MPa, an increase of almost 300%. These results indicate the hydrogel components are penetrating into the BC layer and that both components are necessary to achieve a larger adhesive shear strength than BC alone. The large increase in strength after the infiltration of the PVA-PAMPS hydrogel may be attributed to the hydrogel filling the porous structure of the BC-cement interface (Fig-

ure 3F). The hydrogel may also increase the strength of the interface by bridging the BC network, thereby helping to spread the load across a greater number of BC nanofibers.

The adhesive shear strength can be further improved by performing multiple freeze–thaw cycles on the PVA hydrogel. It has previously been shown that multiple freeze–thaw cycles increase the tensile strength of PVA film.^[54] Therefore, we applied seven cycles of freezing and thawing to the PVA after the infiltration into the BC, and before infiltration of the PAMPS. Multiple cycles of freezing and thawing increase the adhesive shear strength to 2.28 ± 0.27 MPa (see Figure 3G). This is within the

range of the shear strength between cartilage and subchondral bone (2.45 ± 0.85 MPa), indicating the strength of this interface may be sufficient for attachment of the hydrogel to a porous titanium implant that allows for bone ingrowth. We also tested extending the time for diffusing the PVA into the BC layer by heating in the hydrothermal reactor for 3 days instead of 1 day at 110 °C. This processing change did not improve performance, indicating that the PVA is fully diffused into the BC layer within 24 h.

In order to clarify the extent to which the cement improved the adhesion to the BC-PVA-PAMPS hydrogel, we tested control samples in which the titanium plugs were adhered together only with the BC-PVA-PAMPS hydrogel. Figure S6 (Supporting Information) shows an image of the sample before and after shear testing. The fracture surface suggests the hydrogel-titanium sample underwent adhesive failure rather than the cohesive failure exhibited by the samples made with cement. The shear strength was 0.37 ± 0.17 MPa for this hydrogel-titanium sample, 4.6 times lower than the 1.70 ± 0.18 MPa shear strength achieved by using cement to attach the hydrogel to titanium. Thus, the presence of the cement leads to a dramatic enhancement of the adhesive shear strength.

In summary, we have described a new strategy, NEST, for forming bonds to hydrogels three times stronger than the state-of-the-art. NEST involves the formation of an adhesive bond to a nanofibrous sheet in the dry state, followed by the formation of a hydrogel within the nanofibrous sheet. An example of NEST was illustrated using an α -TCP cement containing phosphoserine for adhesion and stainless steel micropowder for reinforcement. The cement undergoes hydrolysis to form hydroxyapatite flakes that mineralize a ≈ 10 -micron-thick layer of the nanofibrous sheet of BC. This bond is strengthened further after infiltration of PVA and PAMPS into the BC sheet, resulting in nanofiber-mediated attachment between the hydrogel and cement. These results show strong bonds to hydrogels can be achieved by mimicking the nanoscale structure of the osteochondral junction, namely the mineralization of the collagen nanofibers that give cartilage its tensile strength. Although we have focused on the use of α -TCP cement, other adhesives and cements may be employed with the NEST strategy. NEST may prove useful for creating hydrogel-capped titanium implants for cartilage resurfacing, in which the porous titanium base facilitates osseointegration and long-term fixation.

Supporting Information

Supporting Information is available from the Wiley Online Library or from the author.

Acknowledgements

This work was supported in part by Sparta Biomedical and a voucher from the Shared Materials Instrumentation Facility at Duke University. B.J.W. has an equity interest in Sparta Biomedical.

Conflict of Interest

This work was supported in part by Sparta Biomedical. B.J.W. has an equity interest in Sparta Biomedical.

Keywords

bacterial cellulose, cartilage, hydrogels, shear strength, α -tricalcium phosphate

Received: June 30, 2020

Revised: August 5, 2020

Published online:

- [1] E. A. Makris, A. H. Gomoll, K. N. Malizos, J. C. Hu, K. A. Athanasiou, *Nat. Rev. Rheumatol.* **2015**, *11*, 21.
- [2] B. M. Devitt, S. W. Bell, K. E. Webster, J. A. Feller, T. S. Whitehead, *Knee* **2017**, *24*, 508.
- [3] J. F. Baumhauer, D. Singh, M. Glazebrook, C. Blundell, G. De Vries, I. L. Le, D. Nielsen, M. E. Pedersen, A. Sakellariou, M. Solan, G. Wansbrough, A. S. Younger, T. Daniels, for and on behalf of the C. M. S. G., *Foot Ankle Int.* **2016**, *37*, 457.
- [4] M. Falah, G. Nierenberg, M. Soudry, M. Hayden, G. Volpin, *Int. Orthop.* **2010**, *34*, 621.
- [5] Y. D. Levy, S. Gortz, P. A. Pulido, J. C. McCauley, W. D. Bugbee, *Clin. Orthop. Relat. Res.* **2013**, *471*, 231.
- [6] P. C. McCulloch, R. Kang, B. J. Cole, *Tech. Knee Surg.* **2006**, *5*, 165.
- [7] J. Farr, G. C. Gracitelli, N. Shah, E. Y. Chang, A. H. Gomoll, *Am. J. Sports Med.* **2016**, *44*, 2015.
- [8] D. Nathwani, M. McNicholas, A. Hart, J. Miles, V. Bobic, *JBJS Open Access* **2017**, *2*, e0011.
- [9] P. Bollars, M. Bosquet, B. Vandekerckhove, F. Hardeman, J. Bellemans, *Knee Surg. Sports Traumatol. Arthrosc.* **2012**, *20*, 1753.
- [10] P. Bowland, E. Ingham, L. Jennings, J. Fisher, *Proc. Inst. Mech. Eng., Part H* **2015**, *229*, 879.
- [11] T. Diermeier, A. Venjakob, K. Byrne, R. Burgkart, P. Foehr, S. Milz, A. B. Imhoff, S. Vogt, *BMC Musculoskeletal Disord.* **2020**, *21*, 261.
- [12] N. Martinez-Carranza, H. E. Berg, K. Hulthenby, H. Nurmi-Sandh, L. Ryd, A. S. Lagerstedt, *Osteoarthr. Cartilage* **2013**, *21*, 739.
- [13] A. Fuchs, H. Eberbach, K. Izadpanah, G. Bode, N. P. Sudkamp, M. J. Feucht, *Knee Surg. Sports Traumatol. Arthrosc.* **2018**, *26*, 2722.
- [14] F. Yang, J. Zhao, W. J. Koshut, J. Watt, J. Riboh, K. Gall, B. J. Wiley, *Adv. Funct. Mater.* **2020**, 2003451.
- [15] P. Kumar, M. Oka, T. Nakamura, T. Yamamuro, J. Delecrin, *Nihon Seikeigeka Gakkai Zasshi* **1991**, *65*, 1070.
- [16] R. A. Chivers, R. G. Wolowacz, *Int. J. Adhes. Adhes.* **1997**, *17*, 127.
- [17] C. Petrov, B. Serafimov, D. L. Kotzev, *Int. J. Adhes. Adhes.* **1988**, *8*, 207.
- [18] K. L. Shantha, S. Thennarasu, N. Krishnamurti, *J. Adhes. Sci. Technol.* **1989**, *3*, 237.
- [19] V. C. Mow, R. Huiskes, *Basic Orthopaedic Biomechanics & Mechano-biology*, Lippincott Williams & Wilkins, Philadelphia, PA **2005**.
- [20] G. P. Maier, M. V. Rapp, J. H. Waite, J. N. Israelachvili, A. Butler, *Science* **2015**, *349*, 628.
- [21] S. Singla, G. Amarpuri, N. Dhopatkar, T. A. Blackledge, A. Dhinojwala, *Nat. Commun.* **2018**, *9*, 1890.
- [22] H. Yuk, C. E. Varela, C. S. Nabzdyk, X. Mao, R. F. Padera, E. T. Roche, X. Zhao, *Nature* **2019**, *575*, 169.
- [23] C. Cui, C. Fan, Y. Wu, M. Xiao, T. Wu, D. Zhang, X. Chen, B. Liu, Z. Xu, B. Qu, W. Liu, *Adv. Mater.* **2019**, *31*, 1905761.
- [24] M. A. North, C. A. Del Grosso, J. J. Wilker, *ACS Appl. Mater. Interfaces* **2017**, *9*, 7866.
- [25] J. Liu, S. Lin, X. Liu, Z. Qin, Y. Yang, J. Zhang, X. Zhao, *Nat. Commun.* **2020**, *11*, 1071.
- [26] H. Madry, C. N. van Dijk, M. Mueller-Gerbl, *Knee Surg. Sports Traumatol. Arthrosc.* **2010**, *18*, 419.
- [27] M. Keeney, A. Pandit, *Tissue Eng., Part B* **2009**, *15*, 55.
- [28] G. E. Kempson, *Ann. Rheum. Dis.* **1982**, *41*, 508.

- [29] M. Sabatini, P. Pastoureau, F. De Ceuninck, *Cartilage and Osteoarthritis*, Vol. 2, Springer, Berlin **2004**.
- [30] C. Flahiff, D. Feldman, R. Saltz, S. Huang, *J. Biomed. Mater. Res.* **1992**, 26, 481.
- [31] K. H. Siedentop, D. M. Harris, B. Sanchez, *Laryngoscope* **1988**, 98, 731.
- [32] H. Nomori, H. Horio, S. Morinaga, K. Suemasu, *Ann. Thorac. Surg.* **1999**, 67, 212.
- [33] L. Sanders, R. Stone, K. Webb, T. Mefford, J. Nagatomi, *J. Biomed. Mater. Res., Part A* **2015**, 103, 861.
- [34] L. Yuan, Y. Wu, J. Fang, X. Wei, Q. Gu, H. El-Hamshary, S. S. Al-Deyab, Y. Morsi, X. Mo, *Artif. Cells, Nanomed., Biotechnol.* **2017**, 45, 76.
- [35] H. Okino, Y. Nakayama, M. Tanaka, T. Matsuda, *J. Biomed. Mater. Res.* **2002**, 59, 233.
- [36] S. T. K. Raja, T. Thiruselvi, G. Sailakshmi, S. Ganesh, A. Gnanamani, *Biochim. Biophys. Acta, Gen. Subj.* **2013**, 1830, 4030.
- [37] D. Lu, Y. Zhang, Y. Li, H. Wang, Z. Shen, Q. Wei, Z. Lei, *Polym. Chem.* **2016**, 7, 1963.
- [38] W. Nie, X. Yuan, J. Zhao, Y. Zhou, H. Bao, *Carbohydr. Polym.* **2013**, 96, 342.
- [39] D. X. Oh, S. Kim, D. Lee, D. S. Hwang, *Acta Biomater.* **2015**, 20, 104.
- [40] A. I. Bochyńska, S. Sharifi, T. G. van Tienen, P. Buma, D. W. Grijpma, *Macromol. Symp.* **2013**, 334, 40.
- [41] S. Balcioglu, H. Parlakpınar, N. Vardi, E. B. Denkbaz, M. G. Karaaslan, S. Gulgen, E. Taslidere, S. Koytepe, B. Ates, *ACS Appl. Mater. Interfaces* **2016**, 8, 4456.
- [42] H. Zhang, T. Zhao, P. Duffy, Y. Dong, A. N. Annaidh, E. O’Cearbhaill, W. Wang, *Adv. Healthcare Mater.* **2015**, 4, 2260.
- [43] L. Ninan, R. Stroshine, J. Wilker, R. Shi, *Acta Biomater.* **2007**, 3, 687.
- [44] C. Fan, J. Fu, W. Zhu, D.-A. Wang, *Acta Biomater.* **2016**, 33, 51.
- [45] R. Flachsman, N. D. Broom, A. E. Hardy, M. G., *Clin. Orthop. Relat. Res.* **2000**, 381, 212.
- [46] U. Kandalam, A. J. Bouvier, S. B. Casas, R. L. Smith, A. M. Gallego, J. K. Rothrock, J. Y. Thompson, C. Y. C. Huang, E. J. Stelnicki, *Int. J. Oral Maxillofac. Surg.* **2013**, 42, 1054.
- [47] A. Kirillova, C. Kelly, N. von Windheim, K. Gall, *Adv. Healthcare Mater.* **2018**, 7, 1800467.
- [48] H. Shao, K. N. Bachus, R. J. Stewart, *Macromol. Biosci.* **2009**, 9, 464.
- [49] J. Zhang, W. Liu, V. Schnitzler, F. Tancret, J.-M. Bouler, *Acta Biomater.* **2014**, 10, 1035.
- [50] U. Gbureck, J. E. Barralet, K. Spatz, L. M. Grover, R. Thull, *Biomaterials* **2004**, 25, 2187.
- [51] R. I. Martin, P. W. Brown, *J. Mater. Sci.: Mater. Med.* **1995**, 6, 138.
- [52] J. E. Barralet, M. Hofmann, L. M. Grover, U. Gbureck, *Adv. Mater.* **2003**, 15, 2091.
- [53] K. S. TenHuisen, P. W. Brown, *Biomaterials* **1998**, 19, 2209.
- [54] T. Fukumori, T. Nakaoki, *J. Appl. Polym. Sci.* **2014**, 131, n/a.